

## Heterogeneous three-dimensional strain fields during unconfined cyclic compression in bovine articular cartilage explants

C.P. Neu<sup>a</sup>, M.L. Hull<sup>a,b,\*</sup>, J.H. Walton<sup>c</sup>

<sup>a</sup> Biomedical Engineering Graduate Group, University of California at Davis, One Shields Avenue, Davis, CA 95616

<sup>b</sup> Department of Mechanical and Aeronautical Engineering, University of California at Davis, One Shields Avenue, Davis, CA 95616, United States

<sup>c</sup> UC Davis Nuclear Magnetic Resonance Facility, University of California at Davis, One Shields Avenue, Davis, CA 95616

Accepted 24 March 2005

### Abstract

Articular cartilage provides critical load-bearing and tribological properties to the normal function of diarthrodial joints. The unique properties of cartilage, as well as heterogeneous deformations during mechanical compression, are due to the nonuniform microstructural organization of tissue components such as collagens and proteoglycans. A new cartilage deformation by tag registration (CDTR) technique has been developed by the authors to determine heterogeneous deformations in articular cartilage explants. The technique uses a combination of specialized MRI methods, a custom cyclic loading apparatus, and image processing software. The objective of this study was to use the CDTR technique to document strain patterns throughout the volume of normal bovine articular cartilage explants during cyclic unconfined compression at two physiologically-relevant applied normal stress levels (1.29 and 2.57 MPa). Despite simple uniaxial cyclic compressive loading with a flat, nonporous indenter, strain patterns were heterogeneous. Strains in the thickness direction ( $E_{yy}$ ) were compressive, varied nonlinearly with depth from the articular surface from a maximum magnitude of 11% at the articular surface, and were comparable despite a 2-fold increase in applied normal stress. Strains perpendicular to the thickness direction ( $E_{xx}$  and  $E_{zz}$ ) were tensile, decreased linearly with depth from the articular surface from a maximum of 7%, and increased in magnitude 2.5-fold with a 2-fold increase in applied normal stress. Shear strains in the transverse plane ( $E_{xz}$ ) were approximately zero while shear strains in the other two planes were much larger and increased in magnitude with depth from the articular surface, reaching maximum magnitudes of 2% at the articular cartilage–subchondral bone interface. In general, strain patterns indicated that cartilage osteochondral explants exhibited depth-dependent nonisotropic behavior during uniaxial cyclic loading. These results are useful in verifying constitutive formulations of articular cartilage during cyclic unconfined compression and in characterizing the micromechanical environment likely experienced by individual chondrocytes throughout the tissue volume.

© 2005 Orthopaedic Research Society. Published by Elsevier Ltd. All rights reserved.

**Keywords:** Articular cartilage; Magnetic resonance imaging; Three-dimensional; Finite deformation; Unconfined compression

### Introduction

Articular cartilage provides critical load-bearing and tribological properties to the normal function of diarthrodial joints. Adult human articular cartilage is often viewed as a two-phase tissue consisting of a solid phase (composed mainly of collagen and proteoglycan) and a

\* Corresponding author. Address: Department of Mechanical and Aeronautical Engineering, University of California at Davis, One Shields Avenue, Davis, CA 95616, United States. Tel.: +1 530 752 6220; fax: +1 530 752 4158.

E-mail address: mlhull@ucdavis.edu (M.L. Hull).

fluid phase (composed of water and electrolytes) [22]. On a microscopic scale, the collagen and proteoglycan content in the tissue varies with depth from the articulating surface. Collagen is the major organic constituent of cartilage and accounts for 15–22% of the wet tissue weight. Collagen content is highest in the surface zone, decreasing by approximately 15% in the middle and deep zones relative to the surface zone. Proteoglycan accounts for 4–7% of the wet tissue weight. In contrast to the distribution of collagen content, proteoglycan content is lowest in the surface zone and increases by approximately 15% in the middle and deep zones relative to the surface zone. Water content distribution throughout the tissue is similar to that of collagen, accounting for more than 80% of the wet tissue weight at the surface and 65% in the deep zone. During the debilitating disease osteoarthritis, cartilage typically shows a decrease in collagen and proteoglycan content, and an increase in water content [30].

Given the nonuniform structure of articular cartilage, it is not surprising that recent investigators documented heterogeneous strains and anisotropic mechanical properties in the tissue [23,29,36]. Two-dimensional (2D) analyses employing video microscopy and image correlation techniques showed strain on the imaged (cross-sectional) cartilage surface to be heterogeneous in the thickness direction. Important aspects and results of these analyses were that: (1) 2D cartilage strains were computed at equilibrium for both confined [29] and unconfined test protocols [23,36], (2) strains in the thickness direction varied as a function of depth, and (3) strains perpendicular to the thickness direction were either generally zero [23,29] or at least an order of magnitude smaller than strains in the thickness direction [34]. Based on these strain fields, it was possible to compute estimates for equilibrium moduli [28,33]. Also, all strain components changed nonlinearly with increasing load [34]. Additional studies note the anisotropy and depth-dependent strains under applied loading [14,15,36].

A recent cartilage deformation by tag registration (CDTR) technique was developed to further investigate heterogeneous and three-dimensional (3D) deformations throughout the volume of bovine articular cartilage explants during unconfined cyclic compression [25]. The technique employs specialized MRI methods to image cartilage tissue at high resolution in undeformed and deformed states. The technique also employs a custom cyclic loading apparatus and image processing software to compute 3D deformation (i.e. strain) fields in the tissue. The technique provides 3D strain data during a physiologically-relevant “dynamic equilibrium” (i.e. a steady-state cyclic load–displacement response) of the cartilage. In particular, large strains (greater than 10%) were observed perpendicular to the tissue thickness direction in some regions during cyclic unconfined compression, which were expected

based on interstitial water flow resulting from rapid loading and unconstrained explant boundaries [1].

One objective of the work reported in this paper was to use the CDTR technique to document 3D strain patterns in normal bovine articular cartilage explants during cyclic unconfined compression at two applied normal stress levels. Cartilage strain patterns resulting from applied normal stresses of 1.29 and 2.57 MPa were investigated to understand load–deformation behavior across the physiological range of stresses developed during walking [6]. Importantly, noninvasive experimental studies of 3D cartilage deformations are ultimately essential to validate mathematical load–deformation models of cartilage [21], characterize the deformation environment for studies of chondrocyte mechanotransduction [12], evaluate cartilage damage [26], and characterize differences between normal and degenerated (e.g., osteoarthritic) tissues.

## Methods

### Sample preparation

Seven adult bovine knee joints were obtained from a local abattoir immediately following death of the animals and used in deformation analyses. The bovine joints were disarticulated, and a single cylindrical osteochondral explant sample was harvested from each tibial plateau beneath the medial meniscus (Fig. 1). No visible signs of joint degeneration (fissures, etc.) were observed in any of the cartilage tissues used in this study. The line *LM* was identified using the most lateral and medial points on the respective surfaces. The line *AP* was identified as perpendicular to *LM* and passing through the midpoint of the line connecting the tips of the tibial eminences. To provide a test sample in a region of the cartilage that is loaded [31], the sample was located in a medial direction along *LM* approximately 75% of the distance from the intersection of *LM* and *AP* to the most medial surface point. The sample was located in an anterior direction parallel to *AP* approximately 25% of the distance from the intersection of *LM* and *AP* to the most anterior surface point. A 10-mm diameter coring reamer (AR-1224S, Arthrex, Naples, FL) was used to extract samples consisting of cartilage (approximately 1–2 mm thick) and subchondral bone (approximately 2–3 mm thick). The articular surface was attached to a freezing stage (CryoHistomat, Hacker Instruments and Industries, Inc., Fairfield, NJ), and a circular saw and custom jig were used to remove subchondral bone producing a surface parallel to the articular surface and a standardized 4 mm thick sample. During all harvesting procedures, phosphate-buffered saline with protease inhibitors (PBS + PI; 1 mM PMSF, 2 mM disodium EDTA, 5 mM benzamide HCL, and 10 mM NEM [7]) was used to rinse and hydrate the sample. Additionally, the local split-line direction (i.e. collagen fiber orientation on the articular surface) surrounding the sample was identified prior to removal from the tibia [4] and the direction was marked on the cartilage surface using India Ink.

### CDTR technique

The CDTR technique [25] was used to determine 3D strain data in each sample during cyclic unconfined compression. The technique determined 3D strain fields in the sample using specialized MRI methods, a custom cyclic loading apparatus, and image processing software. MRI methods, or pulse sequences, were programmed on a Biospec 70/30 system (7.05 T, Bruker Medical GmbH, Ettlingen, Germany) to acquire undeformed and deformed cartilage images (Fig. 2). The delays alternating with nutations for tailored excitation (DANTE) pulse sequence “tagged” or marked regions of the cartilage [20] that were

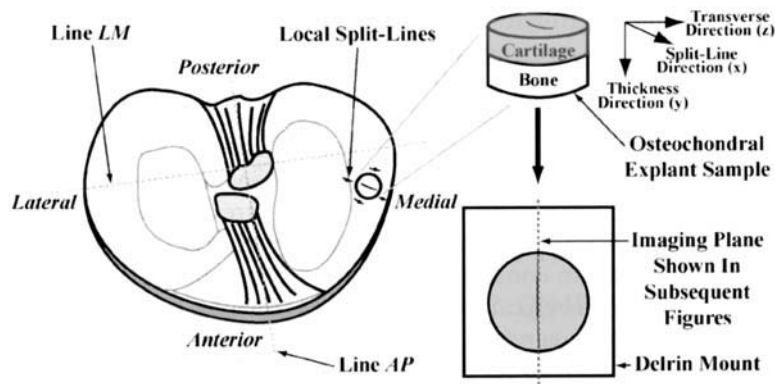


Fig. 1. Diagram showing the osteochondral explant sample harvested from the medial tibial plateau. The sample was secured to a Delrin mount and placed in the cyclic loading apparatus for deformation analyses. The imaging plane shown in subsequent figures was parallel to the local split-line direction of the sample. Compression was in the thickness direction. Lines LM and AP were used to locate the sample.

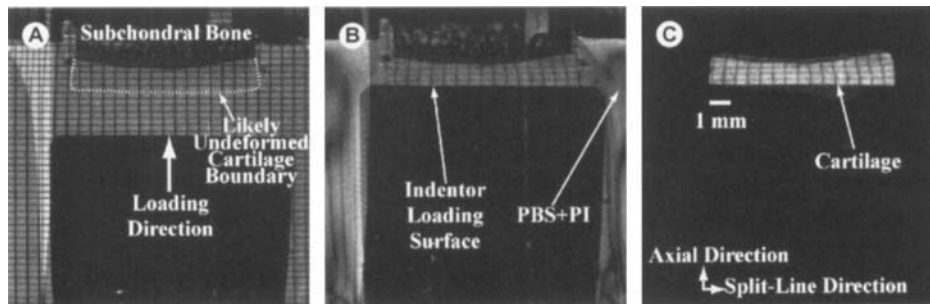


Fig. 2. Images depicting a single undeformed and deformed articular cartilage slice from the center of the 3D volume image. MR images of undeformed cartilage (A; SNR  $\approx$  9.7) and deformed cartilage (B) were acquired through the integration of MRI pulse sequences and a custom cyclic loading apparatus. The deformed cartilage image data (B) was segmented (C) and used in subsequent deformation analyses.

subsequently tracked during compressive loading. The fast spin echo (FSE) sequence imaged the cartilage and tag lines in both undeformed and deformed states. DANTE imaging parameters were: radiofrequency (RF) pulses = 12; RF pulse angle = 15°; RF pulse duration = 8  $\mu$ s; inter-pulse duration = 400  $\mu$ s; magnetic field gradient strength along the cartilage explant thickness = 17.5 G/cm; and transverse magnetic field gradient strength = 10.0 G/cm. FSE imaging parameters were: TR = 4000 ms; effective TE = 12.1 ms; number of echoes per excitation = 4; field of view = 15.3  $\times$  15.3 mm<sup>2</sup>; image matrix size = 256  $\times$  256 pixels<sup>2</sup>; number of averages = 4; and slice thickness = 1.0 mm. A 2D multislice acquisition of 48 total images was acquired with 24 images depicting undeformed cartilage and 24 images depicting deformed cartilage. Of each group of 24 images, two sets of 12 images were acquired as orthogonal planes to allow for a 3D description of deformation. These parameters resulted in multiple images with tag line spacings of 0.4 mm and 0.6 mm in the respective thickness and transverse directions and pixel dimensions of 60  $\times$  60  $\mu$ m<sup>2</sup>. Subsequent to image acquisition, deformed images of cartilage were segmented manually using software employing closed Bezier curves to identify arbitrary object shapes within images (Paravision 3.0, Bruker Medical GmbH, Ettlingen, Germany).

Because the time available for FSE image acquisition was limited by the time duration of the tag lines superimposed by the DANTE pulse sequence (approximately 1 s), MRI and cyclic loading apparatus actions were integrated to acquire MRI data depicting undeformed and deformed cartilage over many loading cycles (Figs. 2 and 3). During each 4-s loading cycle, DANTE tag lines were applied to the cartilage, and portions (i.e. phase encode steps) of undeformed MRI data were acquired. A compressive load was then applied to the sample, followed by acquisition of deformed phase encode steps. A total of 2048 loading cycles were required to obtain all MRI data for each sample which required 2.3 h. During each cycle, a mechanical load of either 79 N or 157 N was applied for a total of 1 s using a flat-surfaced

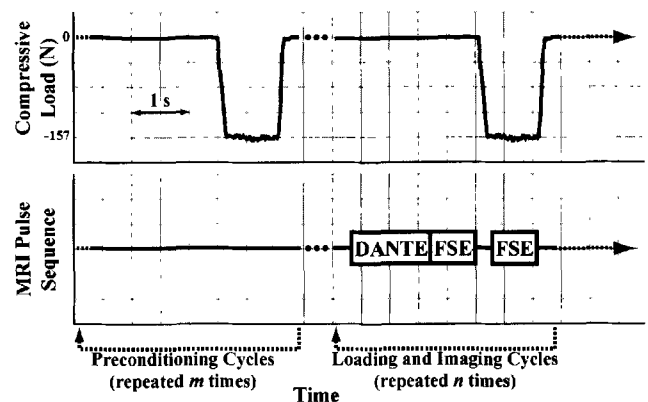


Fig. 3. Timing diagram of the compressive loading and MRI pulse sequence integration. Preconditioning cycles were applied to the cartilage explants prior to MR imaging to reach a steady-state load–displacement response in the tissue and prevent motion artifacts in the images. The DANTE sequence applied a grid pattern of tag lines to the cartilage, while the FSE sequence acquired undeformed image data (prior to compressive loading) and deformed image data (during compressive loading). Compressive loads of 79 N (not shown) and 157 N were applied for 1 s during each 4 s loading cycle. Note that the length of the boxes containing the acronyms DANTE and FSE are not correctly scaled in time.

and non-porous loading platen. Between each loading application, the platen lifted completely off the articular surface. To prevent blur-

ring of images due to any changes in the deformation of the cartilage between load cycles, images were acquired only after the cartilage reached a steady state load–displacement response during the unconfined cyclic compressions [24]. To ensure a steady-state deformation, 100 cyclic loads were applied prior to imaging.

Custom image processing software determined 3D cartilage deformations in MATLAB (v. 6.0, The Mathworks, Natick, MA). Active contours [16,17,35] identified tag line locations in the undeformed and deformed cartilage [25]. The region of interest around the cartilage was enlarged to ultimately facilitate an open cubic B-spline model description of deformation at the tissue boundary using at least two additional contours beyond the boundary [19]. A B-spline model representation of all tag lines was obtained and was governed by control points to allow for the interpolation of any undeformed or deformed location within the cartilage [19]. The position coordinates of each tag line were fit to the B-spline model in a least squares sense [27] using six control points per line. Six control point arrays (corresponding to the three independent split-line, thickness, and transverse directions for each undeformed and deformed volume image) were assembled using B-spline fits of tag line data from multiple images. Finally, strains at deformed locations inside the tissue volume were determined using discrete data interpolated from control points describing material locations in undeformed and deformed states and a maximum likelihood estimation of the deformation gradient tensor  $F$  [10]. The Green–Lagrange strain tensor  $E$  was used to describe 3D strains at each deformed location:

$$E = \frac{1}{2}(F^T F - I) \quad (1)$$

where superscript T is the transpose and  $I$  is the identity tensor. Strain in the split line ( $E_{xx}$ ), thickness ( $E_{yy}$ ), and transverse ( $E_{zz}$ ) directions, as well as shear strains ( $E_{xy}$ ,  $E_{xz}$ ,  $E_{yz}$ ) were computed as a function of position directly as components of the Green–Lagrange strain tensor. Using the imaging and image processing parameters given herein, the error associated with our CDTR technique was 0.83% strain. For further details of the methods used to determine this error, refer to Ref. [25].

#### Experiments and analyses

Two separate deformation analyses were performed on each osteochondral sample. Initially, each sample was secured to a Delrin mount using ethyl cyanoacrylate and placed in the custom apparatus for cyclic loading in unconfined compression [24]. Care was taken to align the split-line direction on the mount so that strain relative to the direction

could be interpreted (Fig. 1). In the first analysis, the CDTR technique was used to obtain 3D strain data throughout the sample at the 79 N load level. The CDTR technique was then used to obtain strain data at the 157 N load level. Despite using a 10-mm diameter coring reamer, calipers measured an  $8.81 \pm 0.07$  mm sample diameter subsequent to harvesting. Thus, the 79 and 157 N loads applied to the cartilage surface using a flat-surfaced and nonporous loading platen resulted in an applied normal stress of 1.29 and 2.57 MPa, respectively, which is within the physiological range during walking [6]. During all experiments, PBS + PI was used to bathe the sample while inside the loading mechanism. Additionally, for one of the samples tested, the heterogeneous spatial distributions of 3D strain fields were visualized in a single slice through the center of the tissue volume for each of the two applied normal stresses. The slice was oriented in the thickness and split-line directions (Figs. 1 and 4).

To characterize 3D strain fields in the entire cartilage tissue volume, strain was computed at locations throughout the cartilage of each sample. Specifically, six independent strain components were computed at 550 locations in each sample. The  $x$  and  $z$  components of 50 locations on an ideal (i.e. 8.8 mm diameter) articular surface were selected using a Gaussian random number generator. Given the experimental alignment protocol (Fig. 1), the surface location coordinates were considered the same for all samples. For each sample, the depth was found along the thickness direction using the segmented deformed images. The same 50 surface locations were then repeated through the (normalized) cartilage depth (from 0% to 100% in 10% increments from the articular surface) for a total of 550 locations per sample. This procedure allowed for the computation of strain components at identical (normalized) locations in each sample. Strain was computed at random rather than particular locations in the  $x$ – $z$  plane because we wanted to determine whether any effects of applied normal stress and/or depth could be generalized to the entire  $x$ – $z$  plane of the articular cartilage.

For each of the six independent strain component datasets, a four-way mixed-effects ANOVA was performed to test the effect of the four experimental factors (i.e. applied normal stress, depth, sample, and location) on strain. Statistical analyses were performed using a statistical software package (SAS v. 8.01, SAS Institute Inc., Cary, NC). Applied normal stress set at two levels (1.29 and 2.57 MPa) and depth set at 11 levels (0–100% in 10% increments) were used as fixed main effects in the model. Cartilage sample and location (in the  $x$ – $z$  plane) were used as random main effects in the model. All interaction effects were investigated except for the four-way interaction between all factors (i.e. applied normal stress  $\times$  depth  $\times$  sample  $\times$  location) because data were not replicated at this level. Both fixed and random main effects were

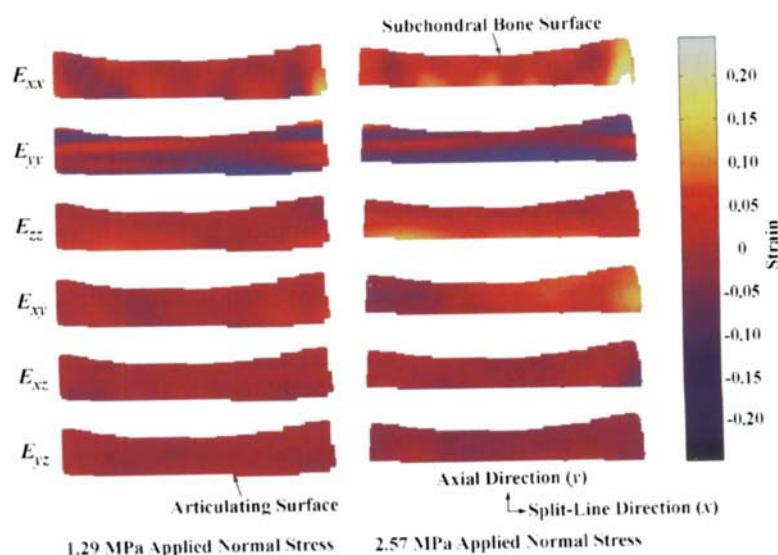


Fig. 4. Example 3D strain fields at two applied normal stress levels. Strain fields are shown in a single deformed articular cartilage slice from the center of the 3D volume image of a typical osteochondral explant sample. In-plane strains ( $E_{xx}$ ,  $E_{yy}$ , and  $E_{xy}$ ) and through-plane strains ( $E_{zz}$ ,  $E_{xz}$ ,  $E_{yz}$ ) exhibited complex and heterogeneous patterns.

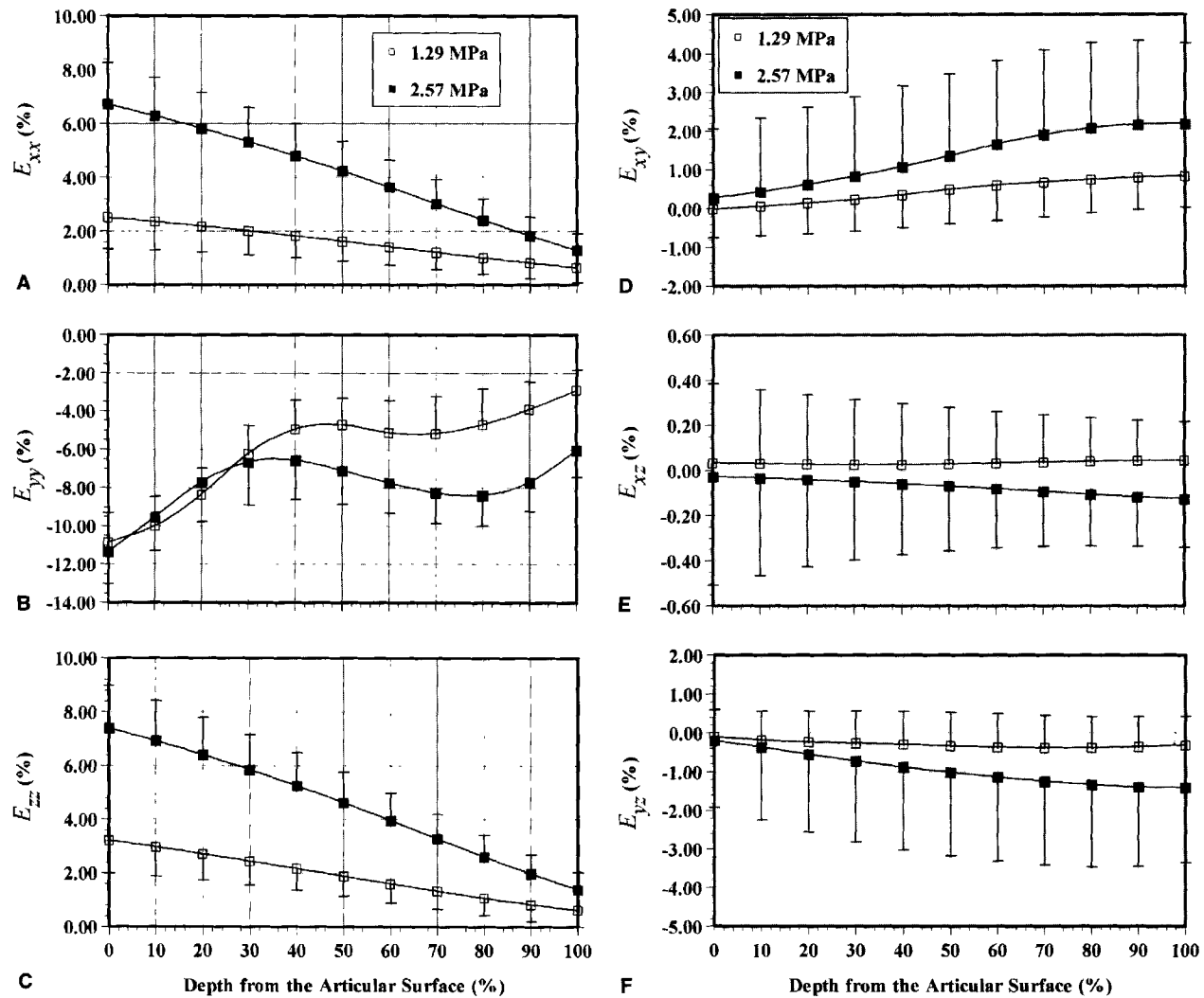


Fig. 5. (A)–(C) Cartilage normal strains in the split-line (A;  $E_{xx}$ ), thickness (B;  $E_{yy}$ ), and transverse (C;  $E_{zz}$ ) directions as a function of depth from the articular surface and applied normal stress. Data is shown as the mean of all 50 locations for all samples in the  $x$ – $z$  plane  $\pm$  one standard error. The strain in the thickness direction  $E_{yy}$  was compressive but was not significantly affected by the applied normal stress. The strains in the other two directions were tensile and increased approximately 2.5-fold for a 2-fold increase in the applied normal stress. (D)–(F) Cartilage shear strains  $E_{xy}$  (D),  $E_{xz}$  (E),  $E_{yz}$  (F) as a function of depth from the articular surface and applied normal stress. Data is shown as the mean of all 50 locations for all samples in the  $x$ – $z$  plane  $\pm$  one standard error. The shear strain in the plane of the cartilage  $E_{xz}$  was approximately an order of magnitude smaller than the other two shear strains particularly at the higher applied normal stress.

included in the ANOVA to determine whether any statistically significant findings for fixed main effects could be generalized to different cartilage samples and locations. Accordingly, only the findings related to the fixed effects were further investigated and presented below.

Significant and important applied normal stress  $\times$  depth interactions for  $E_{xx}$ ,  $E_{zz}$ , and  $E_{yz}$  ( $p < 0.0001$ ) were evident from the ANOVA. Based on the graphically linear trends observed in Fig. 5A and C for  $E_{xx}$  and  $E_{zz}$  respectively, the slope and coefficient of determination for data depicted in these figures were determined using simple linear regressions of mean strain versus depth data. For the shear strain  $E_{yz}$  where the trend in Fig. 5F was nonlinear, the effect of increasing applied normal stress on strain at each depth was further examined using means comparisons at each depth level.

## Results

In a typical sample (Fig. 4), an applied normal stress of 1.29 MPa and 2.57 MPa during unconfined compres-

sion resulted in complex and heterogeneous 3D strains that approached 25% in some regions. Throughout the tissue, strain in the thickness direction ( $E_{yy}$ ) was compressive, and strains in the split-line ( $E_{xx}$ ) and transverse ( $E_{zz}$ ) directions were tensile and varied throughout the tissue. Shear strains  $E_{xy}$ ,  $E_{xz}$ , and  $E_{yz}$  also exhibited noticeable heterogeneous patterns.

Strain in the thickness direction ( $E_{yy}$ ) decreased in magnitude with increasing depth from the articular surface ( $p = 0.0002$ ) (Fig. 5B), but did not depend on the applied normal stress ( $p = 0.1736$ ). Thus, the largest compressive strain magnitudes were observed at the articular surface, and the smallest magnitudes were observed at the cartilage–subchondral bone interface. Although some degree of interaction is evident graphically between the

applied normal stress and depth (Fig. 5B), this interaction was not statistically significant ( $p = 0.1524$ ).

Strains in the split-line ( $E_{xx}$ ) and transverse ( $E_{zz}$ ) directions decreased with increasing depth from the articular surface ( $p < 0.0001$ ) and increased with increasing applied normal stress ( $p \leq 0.0080$ ) (Fig. 5A and C). In general, the largest tensile strain magnitudes were observed at the articular surface and the smallest magnitudes were observed at the cartilage–subchondral bone interface. Strain magnitudes increased linearly with depth from the cartilage–subchondral bone interface ( $r^2 \geq 0.9974$  for all regression lines in Fig. 5A and C), and the slopes of strain versus depth data for the two applied normal stresses were significantly different as indicated by the significant applied normal stress  $\times$  depth interaction ( $p < 0.0001$ ). Furthermore, slopes increased by a factor of approximately 2.5 on average for the 2-fold increase in applied normal stress.

Two of the three shear strains ( $E_{xy}$  and  $E_{yz}$ ) were depth dependent ( $p \leq 0.0153$ ) whereas the third shear strain ( $E_{xz}$ ) was not ( $p = 1.0000$ ), and none of the shear strains were significantly affected by the applied normal stress ( $p \geq 0.1509$ ). Shear strains  $E_{xy}$  and  $E_{yz}$  resulting from the 2.57 MPa applied normal stress increased noticeably in magnitude with depth from the articular surface (Fig. 5D and F). Notwithstanding the significant applied normal stress  $\times$  depth interaction ( $p < 0.0001$ ), means comparisons showed no significant differences between  $E_{yz}$  strain magnitudes resulting from the two applied normal stresses at any particular depth ( $p \geq 0.1538$ ). Shear strain magnitudes for  $E_{xz}$  (i.e. in the plane perpendicular to the loading direction (Fig. 5E)) were approximately an order of magnitude smaller than those for  $E_{xy}$  and  $E_{yz}$  shear strains, particularly at the higher applied normal stress.

In general, strains did not depend on sample ( $p \geq 0.1094$ ). Although normal strains  $E_{xx}$ ,  $E_{yy}$ , and  $E_{zz}$  did not depend on location ( $p \geq 0.1331$ ), shear strains  $E_{xy}$ ,  $E_{xz}$ , and  $E_{yz}$  did depend on location ( $p \leq 0.0339$ ). Furthermore, interactions between the two random factors and between random and fixed factors (e.g. sample  $\times$  depth for all strains) were significant ( $p < 0.05$ ).

## Discussion

This work describes the application of an MRI-based CDTR technique for determining 3D deformations in articular cartilage explants. Strain patterns throughout the volume of normal bovine articular cartilage explants were determined for the first time during cyclic unconfined compression at two applied normal stress levels in multiple samples. Despite the application of simple uniaxial cyclic compression during each loading cycle, strain patterns were heterogeneous. A previous study determined that the strain error for the CDTR tech-

nique was quantified entirely by strain precision because the strain bias was zero [25]. The absolute precision of the CDTR technique was less than 1% strain, enabling a highly detailed description of tissue deformation.

The three normal strains depended on depth but the dependence was different because respective strain components may have been affected by different mechanisms. The strain in the thickness direction ( $E_{yy}$ ) was compressive and varied nonlinearly with depth. This nonlinear relationship may have resulted from the tissue microstructure which is known to be depth dependent [22]. In contrast, strains in the split-line ( $E_{xx}$ ) and transverse ( $E_{zz}$ ) directions were tensile and varied linearly with depth. In addition to tissue microstructure, this linear relationship was possibly the result of the constraint at the cartilage–subchondral bone interface in conjunction with the low aspect ratio (i.e. thickness/diameter) of the sample that was about 1/3. For a sample with a high aspect ratio, the effect of the constraint at the cartilage–subchondral bone interface would have gradually diminished with the distance from this interface.

The result that strains in both the split-line ( $E_{xx}$ ) and transverse ( $E_{zz}$ ) directions showed a strong linear relationship with depth (Fig. 5A and C) suggests that any effect due to friction at the cartilage–platen interface was minimal. A strong influence of friction at the interface would have altered this linear relationship. The minimal effect of friction at the interface was most likely the result of a fluid layer that existed between the platen and articular cartilage when the cartilage was loaded. This layer would have existed because the platen was removed from the articular surface during each load cycle and because the time to develop the applied normal stress was short (<200 ms) (Fig. 3).

An interesting finding was that the strain in the thickness direction ( $E_{yy}$ ) was relatively unaffected by the applied normal stress, whereas the strains in the split-line ( $E_{xx}$ ) and transverse ( $E_{zz}$ ) directions were significantly affected. At each depth, a 2-fold increase in the applied normal stress resulted in a 2.5-fold increase in strain (Fig. 5A and C). When the three normal components of strain are added to estimate the average dilatation, these results indicate that the load support by the interstitial fluid pressurization and solid matrix phases depended on the applied normal stress. For example, the average dilatation at the articular surface was  $-5\%$  for the 1.27 MPa applied normal stress and  $+2\%$  for the 2.59 MPa applied normal stress. Thus the tissue was nearly incompressible for the 1.27 MPa applied normal stress, indicating that the transmitted load was supported primarily by the interstitial fluid pressurization with the remainder supported by the solid matrix. In contrast, the tissue was not compressible for the 2.57 MPa applied normal stress, indicating that load was increasingly supported by the interstitial fluid pressurization. The compressibility of the articular cartilage

evident for the lower applied normal stress may be related to the lower strain rate. Because the loading time was comparable for the two applied normal stresses, the strain rate for the lower applied normal stress was about half that of the higher applied normal stress. These dilatation estimates generally support the hypothesis that fluid pressurization plays an important role in the load-support mechanism of the joint [2].

Unlike previous 2D studies that documented strains perpendicular to the thickness direction either as generally zero [23,29] or at least an order of magnitude smaller than strains in the thickness direction [34], strains perpendicular to the thickness direction reported herein were in general large and on the same order as strains in the thickness direction. This primary difference can be attributed to the loading protocol used (i.e. strain at equilibrium versus strain during cyclic loading). Another study reported that all strain components changed nonlinearly with increasing load [34], which is in contrast to the results reported herein for strain in the split-line and transverse directions. Further, the large strains observed were not unexpected based on rapid loading of the explants (in less than 200 ms [24]) and the resulting pressure gradient in favor of interstitial fluid flow towards the outer boundary of the cylindrical cartilage samples [1].

Shear strains ( $E_{xy}$ ,  $E_{xz}$ ,  $E_{yz}$ ) also exhibited depth-dependent trends (Fig. 5D–F). Shear strain in the  $x$ – $z$  plane (Fig. 5E) was approximately an order of magnitude smaller than other strains. This result in conjunction with the result that  $E_{xx}$  and  $E_{zz}$  were comparable supports the axisymmetry of strain in the  $x$ – $z$  plane. Shear strains  $E_{xy}$  and  $E_{yz}$  increased noticeably with depth from the articular surface (Fig. 5D and F), which was likely a consequence of increased material stiffness due to constraints developed near the cartilage–subchondral bone interface.

Significant effects involving location within the  $x$ – $z$  plane were not unexpected based on likely variations in the microstructural organization of tissue components within each  $x$ – $z$  plane and the altered loading environment that may have occurred at the unconfined sample boundaries. Significant effects involving sample were simply attributed to sample-to-sample variation. Thus, effects involving location and sample did not confound the results that strain magnitudes depended in general on depth and that  $E_{xx}$  and  $E_{zz}$  strain magnitudes depended on applied normal stress.

One application of the results provided herein is to verify constitutive relations for articular cartilage. When observing the depth-dependence of the strain components in conjunction with studies documenting the depth-dependence of the tissue microstructure [22], it is tempting to conclude that the material constitutive relationship is also depth dependent. However caution should be exercised in drawing such a conclusion be-

cause of the constraint developed at the articular cartilage–osteochondral bone interface. While it is difficult to infer constitutive relations from the strain components, nevertheless this study has provided appropriate data including applied normal stresses at the tissue boundary and strain components throughout the volume of the material that may be used to validate previous constitutive relations. Such relations may incorporate transversely isotropic symmetry [5,8,9,18], as well as other formulations [13,32].

Applications of the results reported herein extend beyond the validation of cartilage constitutive relations. Normal 3D deformations may serve as baseline data either in further analyses of cartilage damage [26] or in longitudinal studies of osteoarthritis in animal models [30]. Normal 3D deformations characterize (on a gross level) the deformation environment experienced by individual chondrocytes and thus may indicate that spatially-dependent deformations dominate chondrocyte mechanotransduction [3]. Detailed 3D deformations are also critical for defining requirements for engineered tissues in cartilage repair [11].

While the CDTR technique provided detailed analyses of cartilage strain, limitations existed that must be considered when interpreting these results. First, in our previous study documenting the development of the CDTR technique [25], we reported that strains at the free boundaries (i.e. those that were not attached to bone) were estimated based on extrapolation of tag line data closest to the boundary. Extrapolation was required due to the use of the open cubic B-spline model to describe tissue motion and the inability to segment undeformed cartilage from images. Consequently, the strain (in particular  $E_{yy}$ ) at the articular surface may be an underestimate of the true strain occurring at the boundary. Second, the testing order of the two load levels used was not randomized. Although some concern may arise of carry-over effects between the two experimental tests for each explant, samples were not imaged until a steady-state load–displacement response occurred in the cartilage [24], thus minimizing the potential carry-over effects. A third limitation was associated with the loading protocol. Because restricted time was available for image acquisition, the cartilage had to be rapidly and cyclically loaded. Also to prevent blurring of images, images had to be acquired after the cartilage load–deformation had reached steady state. Thus the strains developed in the cartilage were quasi-static (i.e. developed in the unloaded cartilage due to viscoelastic effects) and dynamic (i.e. due to the cyclic load). Only the dynamic strains and not quasi-static strains were determined by our method. The development of both quasi-static and dynamic strains may be similar to the strains developed during walking where the cartilage would be expected to exhibit a viscoelastic response initially and then reach a steady-state dynamic response

thereafter. However, because the flat indenter applied a uniform stress to an articular cartilage explant, the strains may not translate to an in vivo situation.

In summary, a powerful new MRI-based technique was used to document patterns and magnitudes of strain components throughout the volume of normal bovine articular cartilage explants in unconfined compression. This technique provided all six strain components at any location within the 3D tissue volume with an absolute precision of better than 1% strain. When subjected to simple uniaxial loading in unconfined compression with a flat, nonporous indenter, articular cartilage explants exhibited heterogeneous strain patterns. Strain magnitudes depended on depth, an expected result considering the microstructural organization of cartilage [22] in conjunction with the constraint imposed by the articular cartilage–subchondral bone interface. The largest compressive strain magnitudes (approximately 11%) were observed in the thickness direction ( $E_{yy}$ ) at the articular surface. The largest tensile strains (approximately 7%) were observed perpendicular to the loading direction ( $E_{xx}$  and  $E_{zz}$ ) at the articular surface. The largest shear strain magnitudes (approaching 2%) were observed near the cartilage–subchondral bone interface for  $E_{xy}$  and  $E_{yz}$ . This study demonstrates the importance of noninvasive experimental measures of articular cartilage deformations at physiologically-relevant applied normal stress levels as indicated by both the patterns and magnitudes of strain components.

### Acknowledgments

The authors thank Professor Marc Geers from Eindhoven University of Technology, The Netherlands, for providing his custom strain computation code and Laura Melton for assistance in harvesting cartilage explants. Support from National Science Foundation grants BES-0096436 and OSTI 97-24412 are gratefully acknowledged.

### References

- [1] Armstrong CG, Lai WM, Mow VC. An analysis of the unconfined compression of articular cartilage. *J Biomech Eng* 1984;106:165–73.
- [2] Bachrach NM, Mow VC, Guilak F. Incompressibility of the solid matrix of articular cartilage under high hydrostatic pressures. *J Biomech* 1998;31:445–51.
- [3] Baer AE, Laursen TA, Guilak F, Setton LA. The micromechanical environment of intervertebral disc cells determined by a finite deformation, anisotropic, and biphasic finite element model. *J Biomech Eng* 2003;125:1–11.
- [4] Bullough P, Goodfellow J. The significance of the fine structure of articular cartilage. *J Bone Joint Surg Br* 1968;50:852–7.
- [5] Cohen B, Lai WM, Mow VC. A transversely isotropic biphasic model for unconfined compression of growth plate and chondroepiphysis. *J Biomech Eng* 1998;120:491–6.
- [6] Donahue TL, Hull ML, Rashid MM, Jacobs CR. A finite element model of the human knee joint for the study of tibio-femoral contact. *J Biomech Eng* 2002;124:273–80.
- [7] Frank EH, Grodzinsky AJ, Koob TJ, Eyre DR. Streaming potentials: A sensitive index of enzymatic degradation in articular cartilage. *J Orthop Res* 1987;5:497–508.
- [8] Garcia JJ, Altiero NJ, Haut RC. An approach for the stress analysis of transversely isotropic biphasic cartilage under impact load. *J Biomech Eng* 1998;120:608–13.
- [9] Garcia JJ, Altiero NJ, Haut RC. Estimation of in situ elastic properties of biphasic cartilage based on a transversely isotropic hypo-elastic model. *J Biomech Eng* 2000;122:1–8.
- [10] Geers MGD, De Borst R, Brekelmans WAM. Computing strain fields from discrete displacement fields in 2D-solids. *Int J Solids Struct* 1996;33:4293–307.
- [11] Guilak F, Butler DL, Goldstein SA. Functional tissue engineering: The role of biomechanics in articular cartilage repair. *Clin Orthop* 2001;391(Suppl):295–305.
- [12] Guilak F, Mow VC. The mechanical environment of the chondrocyte: A biphasic finite element model of cell–matrix interactions in articular cartilage. *J Biomech* 2000;33:1663–73.
- [13] Huang CY, Soltz MA, Kopacz M, Mow VC, Ateshian GA. Experimental verification of the roles of intrinsic matrix viscoelasticity and tension-compression nonlinearity in the biphasic response of cartilage. *J Biomech Eng* 2003;125:84–93.
- [14] Jurvelin JS, Buschmann MD, Hunziker EB. Mechanical anisotropy of the human knee articular cartilage in compression. *Proc Inst Mech Eng [H]* 2003;217:215–9.
- [15] Jurvelin JS, Buschmann MD, Hunziker EB. Optical and mechanical determination of Poisson's ratio of adult bovine humeral articular cartilage. *J Biomech* 1997;30:235–41.
- [16] Kass M, Witkin A, Terzopoulos D. Snakes: Active contour models. *Int J Computer Vis* 1987;1:321–31.
- [17] Kumar S, Goldgof D. Automatic tracking of SPAMM grid and the estimation of deformation parameters from cardiac MR images. *IEEE Trans Med Imaging* 1994;13:122–32.
- [18] Lanir Y. Biorheology and fluid flux in swelling tissues. II. Analysis of unconfined compressive response of transversely isotropic cartilage disc. *Biorheology* 1987;24:189–205.
- [19] Mortenson ME. Geometric modeling. New York, NY: John Wiley & Sons, Inc.; 1997.
- [20] Mosher TJ, Smith MB. A DANTE tagging sequence for the evaluation of translational sample motion. *Magn Reson Med* 1990;15:334–9.
- [21] Mow VC, Kuei SC, Lai WM, Armstrong CG. Biphasic creep and stress relaxation of articular cartilage in compression. Theory and experiments. *J Biomech Eng* 1980;102:73–84.
- [22] Mow VC, Ratcliffe A, Robin Poole A. Cartilage and diarthrodial joints as paradigms for hierarchical materials and structures. *Biomaterials* 1992;13:67–97.
- [23] Narmoneva DA, Wang JY, Setton LA. Nonuniform swelling-induced residual strains in articular cartilage. *J Biomech* 1999;32:401–8.
- [24] Neu CP, Hull ML. Toward an MRI-based method to measure non-uniform cartilage deformation: An MRI-cyclic loading apparatus system and steady-state cyclic displacement of articular cartilage under compressive loading. *J Biomech Eng* 2003;125:180–8.
- [25] Neu CP, Hull ML, Walton JH, Buonocore MH. MRI-based technique for determining nonuniform deformations throughout the volume of articular cartilage explants. *Magn Reson Med* 2005;53:321–8.
- [26] Nieminen MT, Toyras J, Rieppo J, Hakumaki JM, Silvennoinen J, Helminen HJ, et al. Quantitative MR microscopy of enzymatically degraded articular cartilage. *Magn Reson Med* 2000;43:676–81.

- [27] Ozturk C, McVeigh ER. Four-dimensional B-spline based motion analysis of tagged MR images: Introduction and in vivo validation. *Phys Med Biol* 2000;45:1683–702.
- [28] Schinagl RM, Gurskis D, Chen AC, Sah RL. Depth-dependent confined compression modulus of full-thickness bovine articular cartilage. *J Orthop Res* 1997;15:499–506.
- [29] Schinagl RM, Ting MK, Price JH, Sah RL. Video microscopy to quantitate the inhomogeneous equilibrium strain within articular cartilage during confined compression. *Ann Biomed Eng* 1996;24:500–12.
- [30] Setton LA, Elliott DM, Mow VC. Altered mechanics of cartilage with osteoarthritis: Human osteoarthritis and an experimental model of joint degeneration. *Osteoarthritis Cartilage* 1999;7:2–14.
- [31] Setton LA, Mow VC, Muller FJ, Pita JC, Howell DS. Mechanical properties of canine articular cartilage are significantly altered following transection of the anterior cruciate ligament. *J Orthop Res* 1994;12:451–63.
- [32] Soltz MA, Ateshian GA. A conewise linear elasticity mixture model for the analysis of tension-compression nonlinearity in articular cartilage. *J Biomech Eng* 2000;122:576–86.
- [33] Wang CC, Chahine NO, Hung CT, Ateshian GA. Optical determination of anisotropic material properties of bovine articular cartilage in compression. *J Biomech* 2003;36:339–53.
- [34] Wang CC, Deng JM, Ateshian GA, Hung CT. An automated approach for direct measurement of two-dimensional strain distributions within articular cartilage under unconfined compression. *J Biomech Eng* 2002;124:557–67.
- [35] Williams DJ, Shah M. A fast algorithm for active contours and curvature estimation. *CVGIP: Image Understanding* 1992;55:14–26.
- [36] Wong M, Ponticello M, Kovanen V, Jurvelin JS. Volumetric changes of articular cartilage during stress relaxation in unconfined compression. *J Biomech* 2000;33:1049–54.